Provided for non-commercial research and education use.
Not for reproduction, distribution or commercial use.

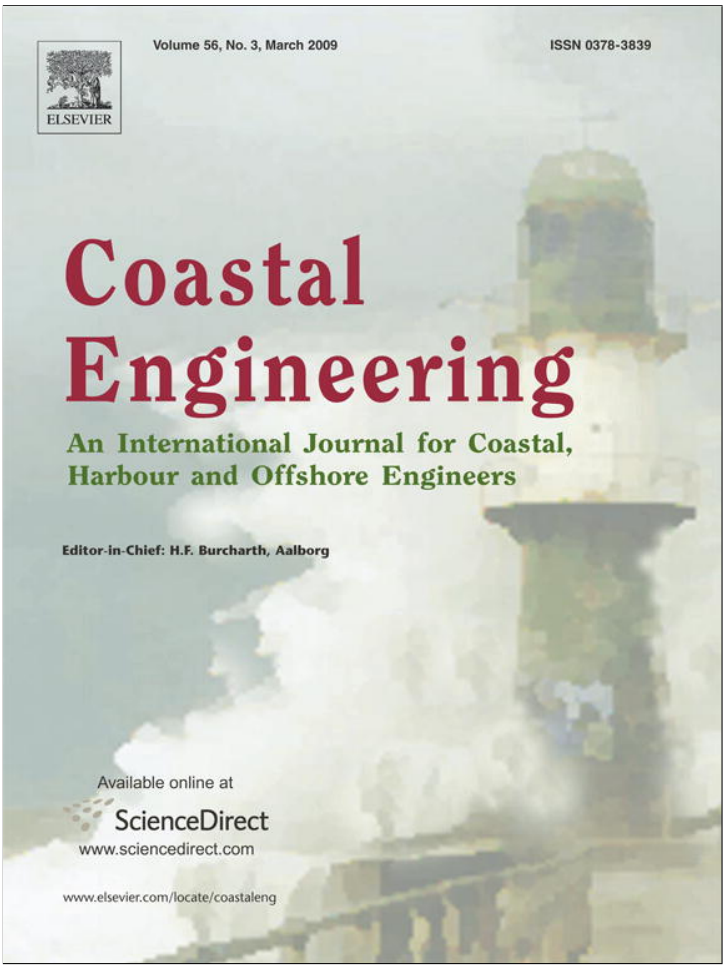

This article appeared in a journal published by Elsevier. The attached copy is furnished to the author for internal non-commercial research and education use, including for instruction at the authors institution and sharing with colleagues.

Other uses, including reproduction and distribution, or selling or licensing copies, or posting to personal, institutional or third party websites are prohibited.

In most cases authors are permitted to post their version of the article (e.g. in Word or Tex form) to their personal website or institutional repository. Authors requiring further information regarding Elsevier's archiving and manuscript policies are encouraged to visit:

http://www.elsevier.com/copyright

Author's personal copy

Coastal Engineering 56 (2009) 320–331

Contents lists available at ScienceDirect

Coastal Engineering

journal homepage: www.elsevier.com/locate/coastaleng

Direct numerical simulations of flow over two-dimensional and three-dimensional ripples and implication to sediment transport: Steady flow

Kiran Bhaganagar [a,*], Tian-Jian Hsu [b]

[a] Department of Atmospheric, Oceanic and Space Sciences, University of Michigan, Ann Arbor, MI 48105, USA
[b] Civil and Environmental Engineering, University of Delaware, Newark, DE 19715, USA

ARTICLE INFO

Article history:
Received 24 June 2008
Accepted 11 September 2008
Available online 28 October 2008

ABSTRACT

A well resolved and highly accurate direct numerical simulation (DNS) solver has been developed to understand the implication of hydrodynamics to sediment transport. In the first part of the study we focus on steady flow over two-dimensional and three-dimensional ripples at two Reynolds numbers Re_τ=180 and 400 (defined by channel half-height and wall-friction velocity) in a channel geometry. The DNS scheme is based on a fourth-order vertical velocity and second-order vertical vorticity formulation, which resolves the difficulties in pressure boundary condition encountered when solving the Navier–Stokes equations. The complex boundary introduced due to the ripples has been imposed in the Cartesian domain using an elegant immersed boundary method. Detailed hydrodynamic analysis has revealed turbulence statistics (in particular, the higher order) and henceforth, the flow structures are sensitive — whether the ripples are two-dimensional or three-dimensional. The importance of fluctuating component of the bottom stress in addition to its mean component; and its significance to sediment transport and ripple migration speed have been investigated.

Published by Elsevier B.V.

1. Introduction

Bedform dynamics is of great importance for fluvial and coastal research. For example, bedform is a major source of energy dissipation of water waves outside the surf zone (e.g., Ardhuin et al., 2002). In the fluvial environments, the migration of river dunes often affects the stability of the river bed and bank (Amsler and Garcia, 1997; Ashworth et al., 2000; Best, 2005), which further causes sedimentation at downstream dams, lakes and river mouth. In typical large-scale fluvial and coastal numerical modeling systems, detailed bedform and wave boundary layer processes cannot be well resolved and the energy dissipation of the overlaying hydrodynamics due to the presence of bedform is parameterized by a friction factor and roughness height.

Accurate prediction of fluvial and coastal hydrodynamics thus depends on detailed understanding and parameterization on the bottom boundary layer processes, including the interactions between the near-bed flow and the bedform (e.g., McLean and Smith, 1979) and wave-current interactions (e.g., Mathisen and Madsen, 1996). Dunes or sand ripple migration is also a major mode of sediment transport in fluvial environment (Best, 2005; Parsons et al., 2005) and under moderate wave energy in the coastal environment (e.g., Traykovski et al., 1999; Hanes et al., 2001). Hence, understanding bedform dynamics is critical in predicting morphodynamics.

Fundamental studies dealing with turbulent flow over rough surfaces have revealed that surface-roughness alters both the first and the higher order statistics significantly (e.g. Perry et al., 1987; Hudson et al., 1996; Antonia and Krogstad, 2001). Furthermore, there is evidence that depending on the geometrical nature of the roughness elements, flow is altered due to roughness both in the inner- as well as outer-layers of the turbulent boundary layer (e.g. George and Simpson, 2000; Bhaganagar et al., 2004, 2007). Our current understanding clearly demonstrates that flow over rough surfaces is complicated and to obtain accurate flow physics, it is essential to perform simulations without a priori assumptions regarding the effect of roughness. Direct numerical simulation (DNS) tool is an ideal choice towards this direction.

In the past, turbulence models have been used to simulate turbulent flows over bedforms. Conventional models based on Reynolds-Averaged Navier–Stokes (RANS) equations (e.g., Chang and Hanes, 2004; Fredsøe et al., 1999) suffer from limitations such as requiring a priori knowledge of flow physics for model closures, low-order accuracy, and over-simplification of flow physics. Due to vastly improved computational capability in recent years, 3-D large-eddy simulations (LES) have successfully demonstrated the superiority over the RANS approach due to less assumptions involved in sub-grid closure (Henn and Sykes, 1999; Calhoun and Street, 2001; Chang and Scotti, 2003a,b; Barr et al., 2004; Yue et al., 2005). This progress is encouraging for further modeling sediment transport because flow turbulence can be more accurately calculated with highly resolved 3-D computations (e.g., Zedler and Street, 2001, 2006; Chang and Scotti, 2003a,b) while inaccuracies may be eventually isolated into more concentrated regime dominated by fluid-

* Corresponding author.
E-mail addresses: kbhagana@umich.edu (K. Bhaganagar), thsu@udel.edu (T.-J. Hsu).

0378-3839/$ – see front matter. Published by Elsevier B.V.
doi:10.1016/j.coastaleng.2008.09.010

Author's personal copy

sediment interactions and inter-granular interactions (e.g., Hsu et al., 2004; Calantoni et al., 2005). This progress also justifies the further use of direct-numerical-simulation (DNS) approach to fully resolve the turbulent flow (and transition to turbulent flow) without any closure approximation. Nevertheless, in the past the well-known limitations of DNS on extensive computational requirements have precluded their widespread use as a practical tool. With the current advances in computational resources, and with novel numerical methods such as immersed-boundary-methods, it is now becoming feasible to use DNS as a research tool for complex geometries (Bhaganagar et al., 2004). The DNS results will provide fundamental understanding of turbulent flow over bedforms, comprehensive database for various flow conditions (De Angelis et al., 1997; Cherukat et al., 1998; Scandura et al., 2000) and improved closures for LES and RANS modeling approaches.

In the natural stream bed and sea-bed, the bedforms are often highly three-dimensional (e.g., Raudkivi, 1997; Traykovski et al., 1999) while existing DNS studies focus on the flow over two-dimensional bedforms (De Angelis et al., 1997; Cherukat et al., 1998; Scandura et al., 2000). Hence, in the present study we first address the difference between the two-dimensional (2-D) and three-dimensional (3-D) bedforms. The DNS model results are used to understand the flow structure due to 2-D and 3-D ripples for two different Reynolds numbers of steady flow by comparing with the corresponding smooth-wall condition. As a preliminary step toward sediment transport modeling, we also investigate the significance of the fluctuating component of the bottom stress (Jensen et al., 1989) in relation to the mean component and its implication of sediment transport (McLean et al., 1994).

We first briefly present the formulation and numerical implementation of a well-resolved, accurate, higher-order DNS that has been developed as a valid tool to understand the physics of turbulent flow over bedforms in Section 2. In Section 3 we discuss the first and higher order statistics and the differences between two-dimensional and three-dimensional ripples, and we focus on the flow structures in the presence of three-dimensional ripples. We then discuss the bottom stress over ripples and the implications to sediment transport. This is followed by a summary in Section 4. This is part-I of our study where we concentrate on the steady flow conditions.

2. Numerical approach

2.1. Derivation of Navier–Stokes equations in vertical velocity–vorticity formulation

In DNS, one seeks for a highly accurate numerical solution of the Navier–Stokes equations by solving these equations exactly without any a priori assumptions or parameterizations (i.e. without any turbulence modeling (Pope, 2000)). In this study, the Navier–Stokes equations are expressed in vertical velocity and vertical vorticity formulation. The vertical velocity and vertical vorticity formulation has been used because of its advantage of eliminating the pressure term from the Navier–Stokes equations while requiring the solution of only two governing equations, namely an evolution equation for the Laplacian of the vertical velocity and an evolution equation for the vertical vorticity. As will be discussed next this formulation leads to reduced storage requirements compared to solutions using the Navier–Stokes equations in primitive variables (e.g., Canuto et al., 1988; De Angelis et al., 1997) or in a vorticity transport formulation (e.g. Rist and Fasel, 1995).

The incompressible Newtonian fluid with viscosity ν is described by the Navier–Stokes equation

$$\frac{\partial u_i}{\partial t} = -u_j \frac{\partial u_i}{\partial u_j} - \frac{\partial p}{\partial x_i} + \frac{1}{Re}\Delta u_i, \tag{1}$$

$$\frac{\partial u_i}{\partial x_i} = 0, \tag{2}$$

with $Re = UH/\nu$ the Reynolds number based on averaged centerline velocity U and channel half-height H. In this study, we define $(x_1, x_2, x_3) = (x, y, z)$ the streamwise, spanwise and wall-normal coordinates respectively, $(u_1, u_2, u_3) = (u, v, w)$ are the respective velocities and p is the total pressure. The last term in Eq. (1) is the viscous term and $\Delta = \left[\frac{\partial^2}{\partial x^2} + \frac{\partial^2}{\partial y^2} + \frac{\partial^2}{\partial z^2}\right]$.

The vertical velocity and vertical vorticity formulation of the Navier–Stokes equations for viscous, incompressible fluid in a channel geometry is derived from the governing Navier–Stokes equations expressed in the classical primitive variable formulation as follows:

The momentum equation can be rewritten into the following form for typical DNS approach (e.g., Cherukat et al., 1998)

$$\frac{\partial u_i}{\partial t} = \epsilon_{ijk} u_j \omega_k - \frac{\partial p}{\partial x_i} + \frac{1}{Re}\Delta u_i, \tag{3}$$

where ϵ_{ijk} is the alternating symbol used in Cartesian tensor notation, (w_1, w_2, w_3) are the corresponding components of vorticity and p is total pressure.

A pressure Poisson equation can be further obtained by taking the divergence of the momentum equation and using the continuity condition as follows:

$$\Delta p = \frac{\partial H_i}{\partial x_i} - \Delta\left(\frac{1}{2} u_j u_j\right) \tag{4}$$

where $H_i = (H_1, H_2, H_3) = u \times w = \epsilon_{ijk} u_j w_k$

To seek for a numerical solution in most DNS studies, the momentum and the pressure Poisson equations with the boundary conditions for the velocity and the pressure are solved. An inherent disadvantage of this formulation is the a priori determination of the pressure boundary condition. This problem can be obviated when the governing equations are expressed in vertical velocity and vertical vorticity formulation (Benney and Gustavsson, 1981).The vertical component of the curl of the Navier–Stokes equations results in an evolution equation for the vertical vorticity, ω_z. Application of the Laplace operator to the momentum equation for the normal component of velocity yields an equation for that component through the use of the momentum and the pressure Poisson equations. The resulting equations are a second order evolution equation for vertical vorticity, ω_z, and a fourth order evolution equation for vertical velocity, w, as,

$$\frac{\partial \omega_z}{\partial t} = H_\omega + \frac{1}{Re}\nabla^2 \omega_z, \tag{5}$$

$$\frac{\partial \nabla^2 w}{\partial t} = H_v + \frac{1}{Re}\nabla^4 w, \tag{6}$$

$$w(\pm 1) = \frac{\partial w}{\partial z}(\pm 1) = 0, \tag{7}$$

$$\omega_z(\pm 1) = 0, \tag{8}$$

where

$$H_v = -\frac{\partial}{\partial z}\left[\frac{\partial H_1}{\partial x} + \frac{\partial H_2}{\partial y}\right] + \left[\frac{\partial^2}{\partial x^2} + \frac{\partial^2}{\partial y^2}\right] H_3 \tag{9}$$

$$H_\omega = \frac{\partial H_1}{\partial x} \tag{10}$$

It is computationally efficient to split the fourth-order equation for w into two second-order equations and solve the resulting system

Author's personal copy

(Bhaganagar et al., 2002). For numerical simplicity the fourth-order vertical velocity Eq. (6) is split into two second-order equations as follows,

$$\frac{\partial \phi}{\partial t} = H_v + \frac{1}{Re}\nabla^4 w, \tag{11}$$

$$\nabla^2 w = \phi, \tag{12}$$

Eq. (11) is the evolution equation for the Laplacian of the vertical velocity (ϕ) and Eq. (12) is an equation for w. Once the normal velocity and normal vorticity are computed, the other components of velocity are solved by using the continuity constraint and the definition of normal vorticity.

2.2. Spatial discretization

In the horizontal x–y directions, the spatial discretization are done using Fourier series expansion assuming periodicity. In the wall-normal z direction the flow is inhomogeneous, and flow near the bedforms needs to be well resolved. Hence high resolution compact finite differences have been used to obtain the spatial derivatives ($\frac{\partial}{\partial z}$). For typical finite difference scheme, the low-wavenumber components are well resolved but resolving high-wavenumber components are difficult due to large truncation error. Therefore in order to obtain high resolution, higher-order finite differences are necessary (Canuto et al., 1988). Alternatively, without increasing the formal order of accuracy, spectral-like resolution can be achieved to compute the spatial derivatives using compact finite differences (for details see Lele, 1992). In addition to having spectral-like resolution, the compact finite differences are computationally efficient as this implementation results in a linear system of equations, that can solved using a tridiagonal solver.

2.3. Time integration: Helmholtz and Poisson equations

To avoid stringent time step restrictions, a semi-implicit time integration has been implemented to integrate the resultant discretized equations. For the nonlinear terms, an explicit low-storage, three-stage, fourth order Runge–Kutta scheme (Williamson, 1980) has been used and for the linear viscous terms, an implicit Crank–Nicholson scheme has been used. The solution at the end of each time-step is the sum of the solution of the explicit part and the implicit part. See Carpenter and Kennedy (1994) for the details of the formulation.

The spatial derivatives in Eqs. (5) and (11) are discretized using Fourier series expansion in the horizontal directions, and using compact finite difference in the wall-normal direction. The time advancement is then performed to the discretized Eqs. (5) and (11) which results in Helmholtz type of equations for ϕ and ω_w (wall-normal vorticity) and a Poisson type of equation for w. The resultant Helmholtz- and Poisson-type of equations are solved using tridiagonal solvers. Using the definition of ω_w and continuity condition u and v are obtained.

2.4. Immersed boundary method

The ripples are introduced into the domain using an immersed boundary method (IBM) (Goldstein et al., 1993; Yusof, 1997; Fadlun et al., 2000) so that the simplicity and efficiency of computation in a Cartesian system is retained. The equations of fluid motion are calculated on the regular geometry of a periodic channel. The ripples are introduced as a virtual boundary σ prescribed within the channel as a function of the streamwise (x) and spanwise (z) variables, such that the active boundary D is given by $D=(x,y,z)|z=\sigma(x,y)$ To enforce the no-slip condition at this virtual boundary, a linear profile is assumed for the streamwise u and spanwise velocity components v between zero at $z=\sigma(x,y)$ and the velocity at a grid point above the virtual boundary. The wall-normal component of velocity is then prescribed from u and v, mass conservation and the no-slip condition. The immersed no-slip boundary is prescribed via a body force term. The definition of the body force term is described as follows. To determine the body force, we employ a first-order temporal discretization of the Navier–Stokes equations:

$$\frac{\mathbf{u}^{n+1}-\mathbf{u}^{n}}{\delta t} + \mathbf{u}^{n}\cdot\nabla\mathbf{u}^{n} = -\nabla\mathbf{p}^{n} + \nu\nabla^2\mathbf{u}^{n} + \mathbf{f}, \tag{13}$$

where $\mathbf{f}=(f_x f_y f_z)$ is the body force, $\mathbf{u}=(u,v,w)$ the velocity vector, $\mathbf{p}$ the pressure, ν the kinematic viscosity, δt the time-step increment, and the superscripts $\mathbf{n}$ and $\mathbf{n}+1$ respectively indicate the current and next time level. On the immersed boundary $\sigma(x,y)$, the velocity is zero, such that:

$$\mathbf{u}^{n+1} = (0,0,0) \tag{14}$$

and we approximate the body force as:

$$\mathbf{f} = \frac{\mathbf{V}-\mathbf{u}^{n}}{\delta \mathbf{t}} + \mathbf{u}^{n}\cdot\nabla\mathbf{u}^{n} + \nabla\mathbf{p}^{n} - \nu\nabla^2\mathbf{u}^{n}, \tag{15}$$

where $\mathbf{V}=(0,0,0)$. The time-dependent body force is applied at a set of two points, the one just below the immersed boundary and the other one just above. When the boundary coincides with the grid, the body force is applied at the boundary and at a point below. This method gives flexibility in choosing the immersed boundary not found in some other methods, since there is no need to line up the boundary with a grid.

3. Results

3.1. Numerical parameters

DNS has been performed for a steady flow over idealized ripples in a channel geometry. The physical dimensions of the channel are as follows: the half-height is 2.5 cm ($H/2$), the streamwise and spanwise domain is 10 cm respectively. The upper surface of the channel is flat (we refer to as the smooth-side) and the two sinusoidal ripples are imposed near the lower surface. The ripples have a height from crest to trough of 0.5 cm, and wavelength of 5 cm. A periodic ripples has been imposed close to the lower-wall of the channel on a virtual no-slip surface σ for 2-D and 3-D ripples respectively as follows:

$$\sigma(x,y) = \sigma_o + h/2\sin(\lambda_x 2\pi x), \tag{16}$$

$$\sigma(x,y) = \sigma_o + h/2\sin(\lambda_x 2\pi x)\sin(\lambda_z 2\pi z), \tag{17}$$

where, σ_o is virtual offset of the immersed boundary, λ_x and λ_z are the streamwise and spanwise wavelengths (peak-peak distance) of the ripple and h is the maximum height of the ripple.

A portion of the computational domain extending from lower-wall $z=0$ to $z=1$ cm in the wall-normal direction is shown in Fig. 1. A spline method was used to interpolate the ripple on to the computational mesh. In the wall-normal direction, non-uniform mesh was used. The grid spacing varied from 0.94 wall-units (corresponding to real length of 0.003 cm) adjacent to the virtual no-slip surface to 6.5 wall-units (corresponding to real length of 0.02 cm) at the centerline. In the horizontal directions, the streamwise and spanwise grid spacing was approximately 15 and 8 wall-units respectively. In this paper, we represent the wall units with superscript +, and the conversion of length scale from physical units (y) to wall units (y^+) is $y^+ = y u_\tau/\nu = (y/H)Re_\tau$.

DNS have been performed for $Re_\tau = 180$ and 400 (Reynolds number based on wall-shear velocity u_τ and channel half-height H) in a periodic channel of streamwise and spanwise size $L_x/H = 4.0$ and $L_z/H = 4.0$, where $2H$ is the distance between the plane walls. Two-dimensional and three-dimensional ripples have been placed on virtual surface near the lower-

Author's personal copy

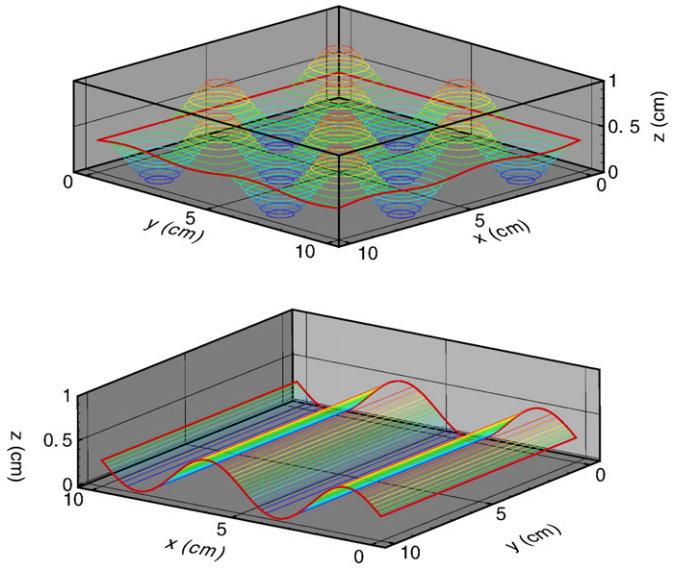

Fig. 1. The computational domain in the lower-half of the channel for flow over 3-D ripples (upper panel) and 2-D ripples (lower panel). The domain contains 2 ripples on the virtual (immersed) surface near the bottom-wall. The total computational domain is $z=5$ cm, $x=10$ cm and $y=10$ cm. The half-height of the channel is at $z=2.5$ cm.

wall and the upper wall is considered to be smooth (i.e., the upper no-slip solid boundary of the computational domain is flat). The spatial discretization used 256 streamwise Fourier modes, 257 wall-normal compact finite-difference grid points of fourth-order accuracy and 256 spanwise Fourier modes. Turbulent initial conditions were imposed for the entire computational domain and the simulations of steady flow over the ripples were performed for sufficiently long time (20–25 non-dimensional time units based on channel half height and u_τ) until converged statistics were obtained. Simulations were performed on a parallel super-computing cluster consisting of thirty-four nodes with wall-clock time of 2 days. Once the velocity field reached a statistically steady state, the computations were continued in time for an additional 10 non-dimensionalized units to obtain mean statistics (which were gathered by averaging over x and y directions as well as in time). For each case, the results obtained from the upper solid-boundary (without ripples) is considered to be the "smooth wall" case, while the results obtained from the lower ripple bed is the corresponding "rough wall" case. The DNS code has been thoroughly validated for channel with rough-walls consisting of three-dimensional egg-pattern roughness elements (Bhaganagar et al., 2004; Sen et al., 2007). The spatial and temporal resolution, grid convergence, turbulence statistics have been validated.

3.2. Computation of u_τ

The wall shear velocity (friction velocity), u_τ is obtained by solving the x (streamwise) momentum equation for the mean velocity,

$$0 = -\frac{\partial p}{\partial x} + \frac{1}{Re}\Delta U + f_1, \tag{18}$$

where, f_1 is the x component of the body force term **f** (refer to Eq. (15)). As the non-dimensional domain extends from $z=-1$ to $z=+1$ in the wall normal direction, integrating the above equation from the lower wall ($z=-1$) to the upper wall ($z=+1$) results in the u_τ at the rough surface as follows:

$$u_\tau = -2\frac{dp}{dx} + \frac{1}{Re}\frac{dU}{dy}|_{z=1} + \int_{z=-1}^{z=1} f_1 dz \tag{19}$$

The last term of the above equation is evaluated using a trapezoidal rule for a non-uniform mesh. For the smooth (flat) upper wall, the friction velocity is expressed as:

$$u_\tau = \frac{1}{Re}\frac{dU}{dy}|_{z=1} \tag{20}$$

u_τ is computed at every x–y grid point, and is averaged over all these locations as well as in time (as the statistics have reached a statistically steady state u_τ does not change significantly with time).

We next compare the turbulence statistics for flow over two-dimensional and three-dimensional ripples at two different Reynolds numbers of $Re_\tau=180$, 400.

3.3. Mean flow velocity

The effects of bedforms/ripples on the statistically-averaged mean flow velocity is generally parameterized based on an equivalent sand grain roughness height (e.g., Grant and Madsen, 1979, 1981). The classical framework established by Nikuradse predicts that the effect of roughness on statistically averaged mean-velocity distribution is confined to a thin wall layer. In the log-region, assuming a logarithmic velocity distribution for flow over a smooth wall is given by,

$$\frac{U}{u_\tau} = \frac{1}{\kappa} ln\left(\frac{z u_\tau}{\nu}\right) + C_0, \tag{21}$$

while the rough-wall modification is

$$\frac{U}{u_\tau} = \frac{1}{\kappa} ln\left(\frac{z u_\tau}{\nu}\right) + C_0 - \frac{\Delta U}{u_\tau}, \tag{22}$$

where, $\Delta U/u_\tau = \Delta U^+ = f(k_s^+)$ is the roughness function with k_s^+ the equivalent sand grain roughness, and we assume $\kappa=0.41$, $C_0=5.5$ is the additive constant for both the rough and smooth wall, u_τ is the local wall-shear velocity (i.e., u_τ of each wall). Comparing the rough- and the smooth-wall distributions, the roughness results in a downward shift of the logarithmic profile with no discernible change in slope.

The boundary layer over a rough surface is characterized by a surface layer, which can be subdivided into the inertial and roughness sublayer (Raupach et al., 1991).The flow in the inertial sublayer is known to be logarithmic, the mean velocity profile can be described by the common logarithmic law:

$$\frac{U}{u_\tau} = \frac{1}{\kappa} ln\frac{(z-\alpha)}{z_o} \tag{23}$$

where z_o is the roughness height and α is the zero-plane displacement which represents the virtual offset due to roughness. It was shown that α and z_o are surface properties determined solely by the roughness geometry and they are obtained by fitting the mean velocity data in the inertial sublayer to the above equation using u_τ as the slope (Cheng and Castro, 2002). The roughness height z_o can be explicitly related to ΔU^+ shown in Eq. (22). Table 1 gives the values of α and z_o for the 2-D and 3-D ripples at $Re_\tau=180$ and 400. They are obtained by fitting the mean velocity to a log-law. Also, shown for comparison are the values of equivalent sand grain roughness in wall units (k_s^+), wall friction-velocity (u_τ) and the bulk or depth averaged velocity (U_b).

Fig. 2 (a) shows the mean velocity profile normalized by the local wall-shear velocity plotted in wall units for the smooth-wall side and rough-wall side for 2-D and 3-D ripples for $Re_\tau=180$. In this figure z^+ represents the distance from the wall in wall units. As seen from the figure, the presence of ripples result in a downward shift in U^+. There is no discernible difference between the 2-D and the 3-D ripples. Similar analysis is repeated for $Re_\tau=400$ and the results are shown in Fig. 2 (b).

Author's personal copy

Table 1
For 2-D and 3-D ripples at $Re_\tau = 180, 400$, the values of virtual offsets (α) and roughness height (z_o) obtained by fitting the mean velocity to a log-law, equivalent sand grain roughness in wall-units (k_s^+), wall friction-velocity (u_τ) and bulk velocity (U_b)

Cases	Re_τ	α/H	z_o/H	k_s^+	u_τ(cm/s)	U_b(cm/s)
2-D ripple	180	0.08	5.34e−3	48	1.36	12.79
3-D ripple	180	0.08	9.81e−3	53	1.51	12.22
2-D ripple	400	0.12	1.2e−2	80	2.1	13.12
3-D ripple	400	0.12	2.9e−2	103	2.71	10.83

Unlike the previous case, noticeable differences to some extent are observed. It appears that as Re increase further, the mean velocity will be sensitive if the ripples are 2-D or 3-D. The magnitude of ΔU^+ for $Re_\tau = 180$ and 400 is 6.0 and 7.4 respectively. These values are consistent with values presented by Raupach et al. (1991) for corresponding equivalent sand grain roughness in wall-units of 48 and 80 respectively for 2-D roughness elements. It serves as a good validation for our numerics. According to Eq. (22), for a fully-rough case (when the equivalent sand grain roughness is greater than 70) the calculated $k_s(30z_o)$ is around 50% of ripple height, which is consistent with field observations. Further work needs to be performed to obtain a relation of the roughness height as a function of the ripple parameters.

Fig. 3 shows the mean streamwise velocity profile scaled by shear velocity of the upper smooth-wall for 2-D and 3-D ripples at $Re_\tau =$ 180,400. Due to the presence of ripples in the lower solid-boundary, the location of peak mean-velocity shifts from the center of the channel towards the upper-half of the channel resulting in loss of symmetry. No discernible differences are observed between the 2-D and the 3-D ripples. Similar trend is observed for the $Re_\tau = 180$ case. Note that the domain above the virtual offset has been not been shown in all the horizontally averaged profiles as the solution below the ripple (inside the ripple) is not physically meaningful for immersed boundary method approach. The dashed line corresponds to the virtual origin.

A characteristic recirculation region downstream of the crest is observed when examining the mean streamwise velocity averaged over the y planes (figure not shown). The velocity gradients are very large near the weather-side of the ripple crest, suggesting a strong bottom stress, while the magnitude of velocity and velocity gradient are smaller at the lee-side and the trough regime of the ripples. These flow characteristics may have important implications to sediment transport processes, which will be discussed in more details in Section 3.6.

3.4. Root-mean-square velocity and vorticity fluctuations

To represent accurate flow physics in turbulence modeling as well as in modeling of mixing/transport processes of the sediment, it is important to account for higher order flow statistics. We are particularly interested in the turbulent intensities (root-mean-square of velocity fluctuation and vorticity fluctuations) in the turbulent boundary layer, since behavior of the former allows us to infer how presence of ripples affects the largest scales of motion, while that of the latter indicates how it alters the small-scale turbulence features.

Fig. 4 shows the r.m.s. of u streamwise velocity fluctuations for 2-D and 3-D ripples at two different Reynolds number of $Re_\tau = 180$ and 400. Comparing with the upper smooth wall condition, both 2-D and 3-D ripples conditions exhibit an increase of turbulence intensity above the ripple crest as the Reynolds number increases, and this is in agreement with our existing knowledge of turbulent flow over rough surfaces (Bandyopadhyay and Watson, 1988; George and Simpson, 2000; Antonia and Krogstad, 2001; Ashrafian et al., 2004). On comparing the 2-D and 3-D ripples at $Re_\tau = 180$ we observe the peak r.m.s. value for 3-D case is higher compared to the 2-D case, and differences between the two are apparent throughout the boundary layer. For 3-D ripple, the r.m.s. of u velocity is larger than that of 2-D ripple below the ripple crest. On the other hand, above the ripple crest the r.m.s of u velocity is smaller for 3-D ripple condition. Also notice that for 2-D ripple the location of the minimum of r.m.s. of velocity fluctuations shifts from the center of the channel to upper side of the channel, suggesting different roughness

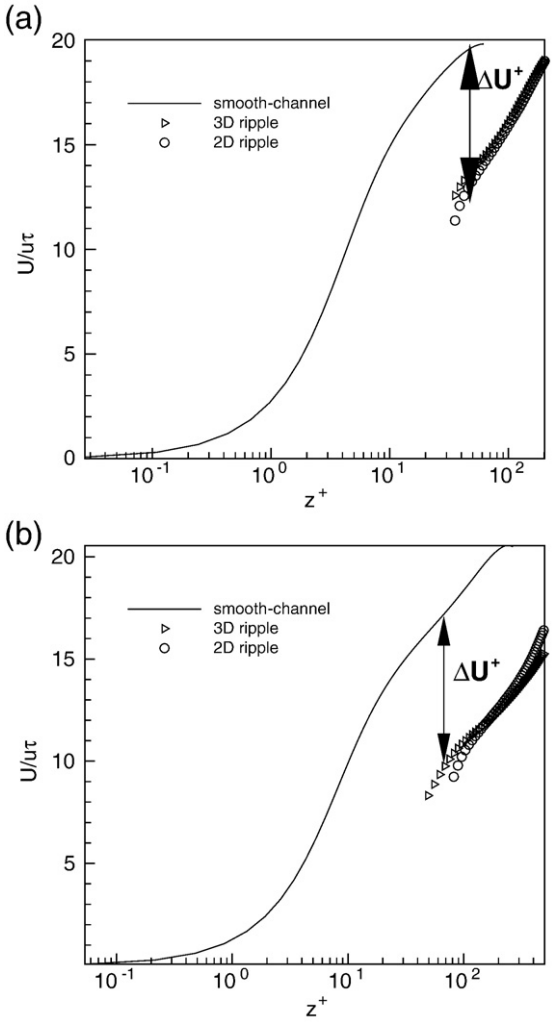

Fig. 2. Mean velocity profile normalized by the local u_τ shown for the smooth-wall, 2-D and 3-D ripples plotted in wall-units at (a) (upper panel) $Re_\tau = 180$ and (b) (lower panel) $Re_\tau = 400$.

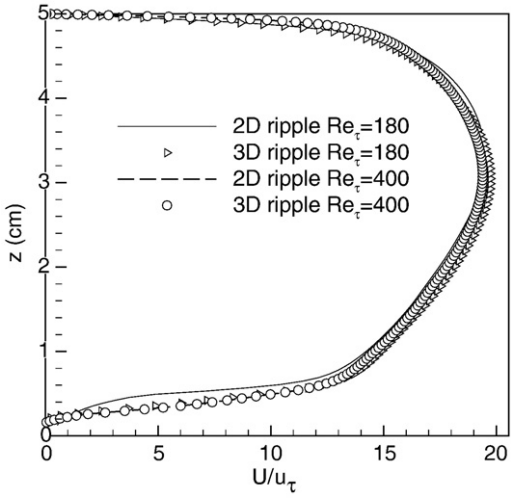

Fig. 3. Mean velocity profile normalized by u_τ for smooth wall shown for 2-D and 3-D ripples at $Re_\tau = 180$ and 400.

Author's personal copy

thicknesses. A similar trend is observed for Re_τ=400. In fact, the difference in magnitude of the r.m.s. of streamwise velocity fluctuation appears to be more pronounced when the Reynolds number is higher. Fig. 4 b and c presents the r.m.s. of w wall-normal and v spanwise velocity fluctuations respectively. Comparing with the upper smooth-wall, there is again an increase of the turbulence intensity due to ripples. The difference in the magnitudes is apparent throughout the boundary layer between the 2-D and 3-D ripples. However, unlike the peak r.m.s of

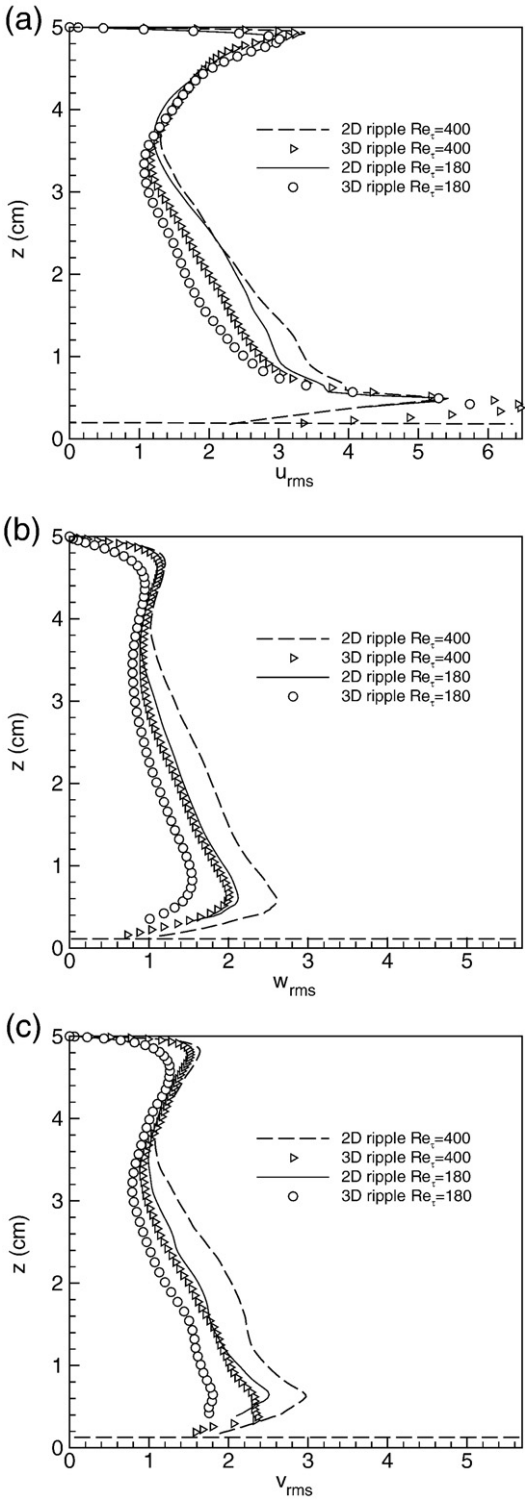

Fig. 4. Turbulent intensity of velocity (cm/s) of (a) (upper panel) streamwise (b) (middle panel) wall-normal and (c) (lower panel) spanwise components plotted vs. the distance from the wall for the 2-D and 3-D ripples at Re_τ=180, 400.

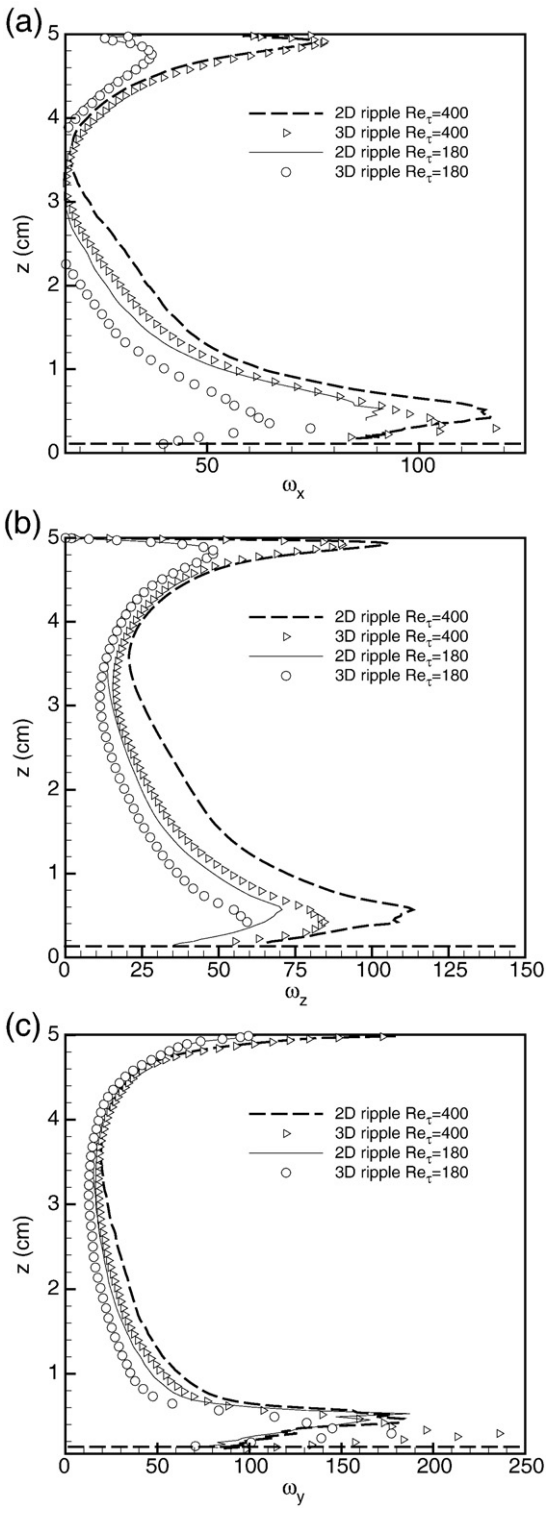

Fig. 5. For the 2-D and 3-D ripples at Re_τ=180 and 400, the r.m.s. of (a) (upper panel) streamwise component (b) (middle panel) wall-normal component and (c) (lower panel) spanwise component of vorticity fluctuations (s^{-1}).

u fluctuations (Fig. 4a), the peak r.m.s. of v and w fluctuations are larger for 2-D ripple than that of 3-D ripple. These results indicate that the three components of velocity fluctuations are rather anisotropic. This trend is more apparent close to the bedform. Ripple bed modifies the large scale features of the flows and significant differences are discernible between the 2-D and 3-D ripples both in the vicinity of the ripple bed as well as away from the wall layer.

Author's personal copy

The behavior of the small scale turbulence is revealed by the vorticity fluctuations presented in Fig. 5 a, b and c. The r.m.s. of streamwise (ω_x), wall-normal (ω_z) and spanwise (ω_y) vorticity fluctuations are shown for both 2-D and 3-D fluctuations at the two Reynolds number of $Re_\tau = 180, 400$. Comparing with the upper smooth wall, the intensity of ω_x and ω_y increases due to the ripples, while intensity of ω_z is similar between the upper smooth-wall and lower ripple-bed. On comparing the 2-D and 3-D ripples, magnitude of peak value is higher for 2-D compared to the 3-D for r.m.s. of ω_x and ω_z fluctuations. Furthermore, significant differences between the 2-D and 3-D ripples are observed for the spanwise ω_y fluctuation close to the ripple surface. These differences gradually fade as we move away from the ripple surface. These results indicate that the ripples modify the small scale features of the flow as the three components of vorticity fluctuations are enhanced due to the ripple. Substantial differences are observed between the 2-D and 3-D ripples in both the small-scale features and large-scale features of the turbulent flow.

3.5. Turbulence structures

We are interested to analyse the modification of the turbulence structures due to the presence of ripples compared to smooth (flat) wall. For this purpose, we focus on specific case of three-dimensional ripples at $Re_\tau = 400$.

We examine the velocity and vorticity structures in x–z and y–z planes. Fig. 6 is contour plot of u, w and v velocity fluctuations in x–z plane. The u structure reveal an alternating positive and negative patters. These structures are of much larger scale near the ripples compared to the smooth wall. Similar trend is observed in both w and v fluctuations. The structure of w component of velocity shows an increased activity in the rough-wall side of the channel, and the angle of inclination of the structures also differs. Fig. 7 is a contour plot of ω_x, ω_z and ω_y vorticity fluctuations in the x–z plane. The ω_y contours show that an irregular pattern of structures is present above the peak locations of the rippled surface. The turbulence above the ripples affects the vorticity on the ripples. The ω_z contours show an organized, alternating pattern of dominant vorticity close to the ripple. A similar pattern is observed for the ω_x fluctuations. Fig. 8 presents the instantaneous velocity v–w vectors superimposed on u contours in the y–z plane. Large scale streamwise rolls are observed near the rough wall compared to the smooth wall.

Based on analysis of the turbulence statistics and the turbulence structures, we conclude that rippled surface results in an enhanced and more energetic turbulence structures with an increased turbulence activity compared to a flat surface. Further, the kinematics (2-D or 3-D ripples) also plays an important role, in addition to the dynamics (turbulence) in altering the flow characteristics. The higher order statistics and hence the nature of the flow structures are more sensitive whether the ripples are two-dimensional or three-dimensional. This implies that 2-D and 3-D ripples have a different effect on the sediment transport. In the next two sections, we concentrate on the implications of sediment transport from a perspective of bottom stress which may be further used to infer bedload transport. Both bottom stress and turbulence structure are also expected to affect suspended load transport. Direct modeling of suspended load transport is necessary and will be pursued as future work.

3.6. Bottom stress over ripples

Snapshots of the spatial distribution of streamwise bottom shear stress τ_{bx} over the 2-D and 3-D ripples are shown in Figs. 9 and 10. In the present DNS study, the instantaneous bottom stress is calculated directly at the ripple surface and hence $\tau_{bx} = \mu \frac{\partial u}{\partial z}$, where μ is the dynamic viscosity. The streamwise bottom stress τ_{bx} at the weather-side of the ripple is positive, i.e., following the direction of the steady current. On the other hand, due to the separation bubble, τ_{bx} at the lee-side of the ripple is mostly negative and the magnitude is also smaller compared to that at the weather-side.

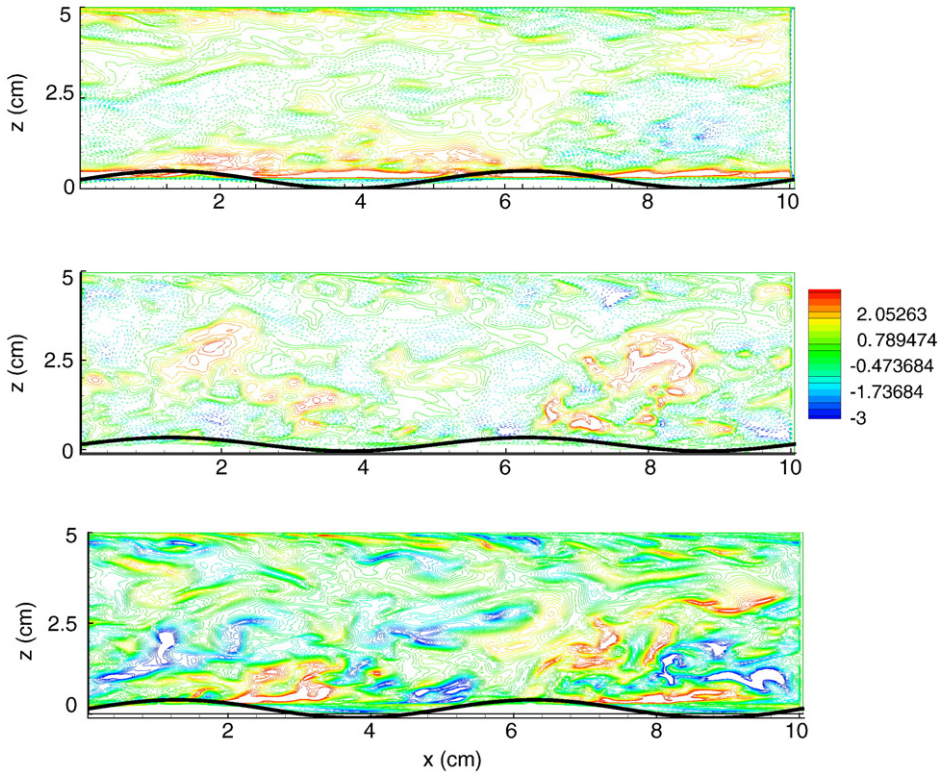

Fig. 6. Velocity fluctuations scaled by u_τ in the x–z plane (a) (upper panel) u streamwise velocity fluctuations, (b) (middle panel) w wall-normal velocity fluctuations, (c) (lower panel) v spanwise velocity fluctuations.

Author's personal copy

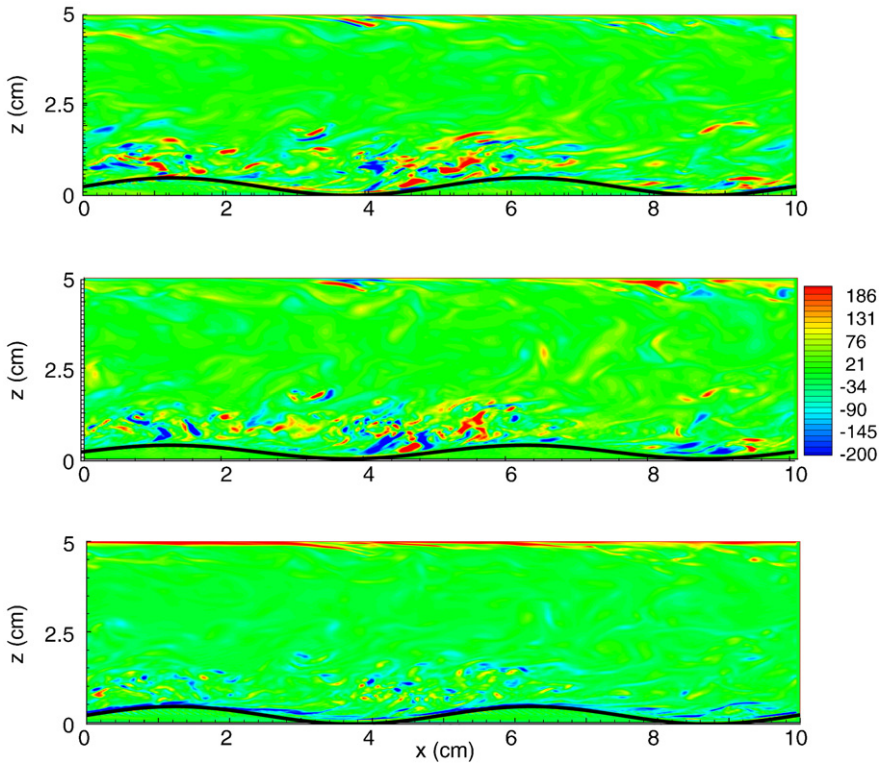

Fig. 7. Vorticity fluctuations normalized by u_τ in the x–z plane (a) (upper panel) ω_x, (b) (middle panel) ω_z, (c) (lower panel) ω_y vorticity fluctuations.

In turbulent flow, the instantaneous velocity can be separated into mean and fluctuating components. In this study, we consider steady flow over ripple and hence the overbar represents the time-averaged quantity. Because the bottom stress is in direct response to the overlaying turbulent flow, the bottom stress can also be decomposed into mean and fluctuating components in boundary layer study (Jensen et al., 1989; Fredsøe et al., 2003):

$$\tau_{bx} = \overline{\tau}_{bx} + \tau'_{bx} \tag{24}$$

Therefore, we calculate

$$\overline{\tau}_{bx} = \mu \frac{\partial \overline{u}}{\partial z}; \tag{25}$$

$$\tau'_{bx} = \mu \frac{\partial u'}{\partial z} \tag{26}$$

Here, $\overline{u}$ represents the time-averaged mean velocity and u' is the fluctuating component (deviation from the mean).

The magnitude, temporal patterns and spatial distribution of the bottom stress are critical in determining the sediment transport. The transport that occurs within few grain diameters above the bed is directly in response to bottom stress. This is often referred as bedload. The transport that occurs more away from the bed, i.e., the suspended load, is strongly affected by the turbulent flow patterns (Zedler and Street, 2006). However, the bottom reference concentration (e.g., Engelund and Fredsøe, 1976) or pick-up function (Van, 1984) required in the suspended load model is also parameterized by bottom stress. Therefore, by examining the spatial and temporal distribution of bottom stress over the ripples, it is possible to understand at least qualitatively some morphodynamic features of ripples, such as migration speed (e.g., McLean et al., 1994).

It is a common practice to represent sediment transport by nondimensionalizing the bottom stress as the Shields parameter:

$$\theta = \frac{\tau_b}{\rho(s-1)gd} \tag{27}$$

where d is the grain diameter, s is the specific gravity of the sediment and ρ is the fluid density. For small ripples, the ripple dimensions are determined by the grain size (Raudkivi, 1997). Here, in order to further interpret the DNS results for sediment transport, we consider fine sand grain of specific gravity s=2.65 and diameter d=0.1 mm. This

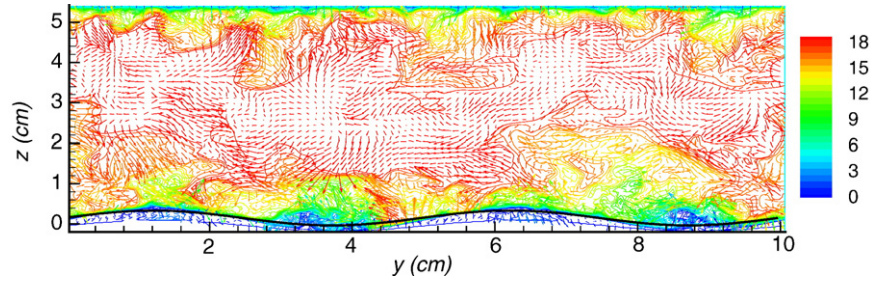

Fig. 8. Instantaneous v–w velocity vectors superimposed on u velocity shown in the y–z plane. All the velocity components have been scaled with u_τ and are dimensionless.

Author's personal copy

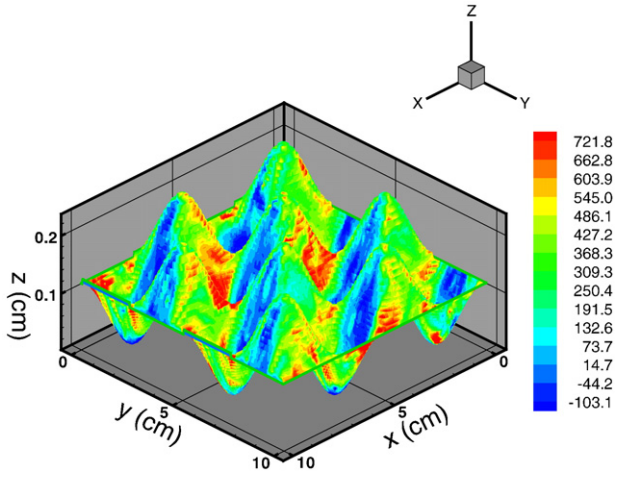

Fig. 9. The instantaneous bottom stress (dimensionless as it is scaled by u_τ and half-height of the channel, H) along the ripple surface for the 3-D ripple.

choice of grain size is consistent with laboratory and field observations of sand ripple dimensions (e.g., Mantz, 1978; Wiberg and Harris, 1994) similar to the ones we considered in this paper.

Fig. 11 presents a 2.2-second realization of the instantaneous nondimensionalized bottom stress at the ripple crest (Fig. 11 a) and trough (Fig. 11 b) for the 3-D ripple case. The time-averaged mean Shields parameter is 0.218 (dashed line in Fig. 11 a) at the ripple crest consistent with the general observation that ripple bed exist when the Shields parameter is smaller than unity. Notice that the time-averaged Shields parameter at the ripple trough is only −0.0163. Because the critical Shields parameter is about θ_c=0.08 according to Shields diagram, suggesting that there is almost no transport at the ripple trough. This is also consistent with the general observation that the bottom stress at the lee-side of the ripple/dune is small due to flow separation (e.g., Tjerry and Fredsøe, 2004).

Fig. 12 further presents a similar realization of the instantaneous nondimensionalized bottom stress at the ripple crest (Fig. 11a) and trough (Fig. 11b) for the 2-D ripple case. In terms of the time-averaged Shields parameter, there is not much difference between the 2-D and 3-D ripples. The time-averaged Shields parameter at ripple crest is 0.216, rather close to that of the 3-D ripple. The time-averaged Shield parameter at the ripple valley is −0.0413. Its magnitude is somewhat larger than that of 3-D ripple but remains to be small in terms of transport intensity. However, the fluctuating component of the Shields parameter (τ_b') are quite different between the 2-D and 3-D ripple cases. The fluctuating component of the Shield parameter is significantly larger for 3-D ripple (r.m.s. value 0.0332 at crest and 0.0418 at trough) than that of the 2-D ripple (r.m.s. value 0.0085 at crest and 0.0218 at trough). This can be directly attributed, perhaps, to larger turbulent fluctuation levels of the 3-D ripple (see Fig. 4a). Because the fluctuating bottom stress and turbulence intensity (streamwise direction) are both much larger in 3-D ripple, it is reasonable to expect the suspended load transport to be affected by these features.

3.6.1. Implication to ripple migration

Using the bottom stress calculated by the DNS for 2-D and 3-D ripples, we can qualitatively estimate the local sediment transport rates. We note here that a complete calculation of sediment transport of sand ripple requires additional governing equations for sediment concentration and velocity. This is not yet developed in this study. However, to make use of the detailed bottom stress information obtained from DNS, we will adopt a simple theory for sediment transport in order to study its implication for ripple migration speed.

Following Tjerry and Fredsøe (2005), we consider a train of ripples of identical shape migrating at a constant speed driven by a steady current. The shape of the ripple is described by a given function $h(x,t)$ with height H_r, and length L_r. The shape of the migrating ripple is assumed to be in equilibrium, namely, the ripples move with a permanent shape and a constant speed a in the x-direction:

$$h = h(x-at) \tag{28}$$

It is often assumed that the net transport in the trough regime is negligible at the ripple crest. Significant (or the entire) amount of sediment that is transported over the crest is also assumed to be deposited at the lee-side of the ripple. Under these assumptions, the transport rate at the crest is defined here as q_r and is considered to deposit completely at the lee-side of the ripple. Using q_r, and the ripple height H_r, the ripple migration speed can be determined through mass conservation (Tjerry and Fredsøe, 2005):

$$a = \frac{q_r}{H_r(1-n)} \tag{29}$$

where, n=0.37 is the porosity of the sand bed. Eq. (29) requires an estimate of q_r in order to calculate ripple migration speed. Tjerry and Fredsøe (2005) assume the transport rate can be directly parameterized by local bottom stress (i.e., bedload assumption, see also Andersen (2000) for the implementation in Dune2D), the nondimensionalized transport rate can be calculated by a power law (Meyer-Peter and Muller, 1948):

$$\psi_c = \frac{q_r}{\sqrt{(s-1)gd^3}} = 8(\theta-\theta_c)^{3/2} \tag{30}$$

The net transport rate at the ripple crest for 3-D ripple over the given 2.2-seconds bottom stress realization (Fig. 11) is qr=6.661e−6 m^2/s, while the net transport rate at the valley is −1.244e−8 m^2/s. This is consistent with the assumption used in Eq. (29) that the transport in the trough regime is negligible. The migration speed estimated using Eq. (29) for 3-D ripple is a=0.212 mm/s(0.76 m/h). On the other hand, using the 2-seconds bottom stress realization for 2D ripple, the net transport rate at the 2D ripple crest is qr=6.414e−6 m^2/s which is very close to that of the 3-D ripple because the time-averaged bottom stress for 2-D and 3-D ripple cases are similar. The net transport rate for 2-D ripple at valley is again small (−4.022e−9 m^2/s). The migration speed for 2-D ripple estimate from Eq. (29) is a=0.204 mm/s (0.733 m/h), which is only

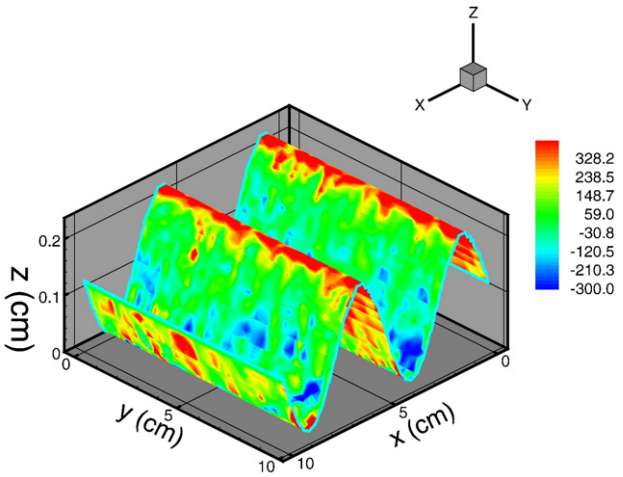

Fig. 10. The instantaneous bottom stress (dimensionless as it is scaled by u_τ and H) along the ripple surface for the 2-D ripple.

Author's personal copy

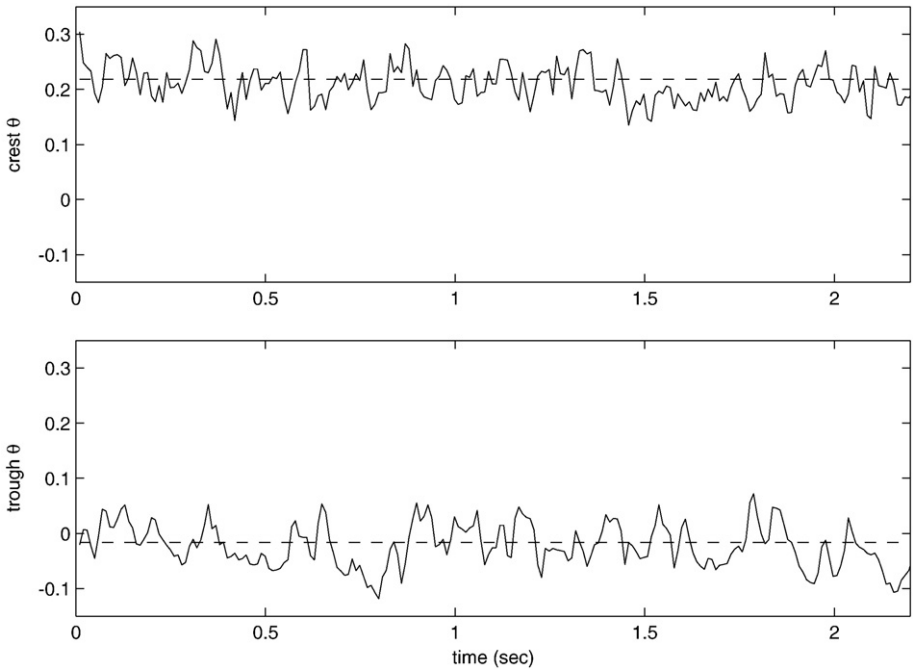

Fig. 11. Shields parameter (nondimensionalized bottom stress) at 3-D ripple crest (upper panel) and ripple trough (lower panel). Three-dimensional ripple with sand grain diameter 0.1 mm (assumed grain size for typical ripple dimension studied here).

slightly smaller than the migration speed of the 3-D ripple under the same flow condition.

Kuhlborn (1993) proposed an empirical formula for estimating the migration speed of ripples (see also Raudkivi, 1997):

$$V_r = 2.1\left(\frac{\theta}{\theta_c}\right)^{2.42} - 2.1. \tag{31}$$

Taking the critical Shields parameter $\theta c = 0.08$, the migration speeds of the 2-D and 3-D ripples are calculated to be 0.022 m/h and 0.021 m/h, which are much smaller than that estimated by DNS bottom stress and bedload formula. We must note here that the empirical estimation of migration speed shown in Eq. (31) is rather sensitive to grain size, which appears to be consistent with laboratory observation (Baas and Koning, 1995). Additionally, such large difference in estimated migration speed may imply that ripple migration for such fine sediment is dominated by suspended load.

We comment here that because the time-averaged bottom stress for 2-D and 3-D ripple are similar, their resulting migration speeds based on simple power-law type approach is also similar. However, it

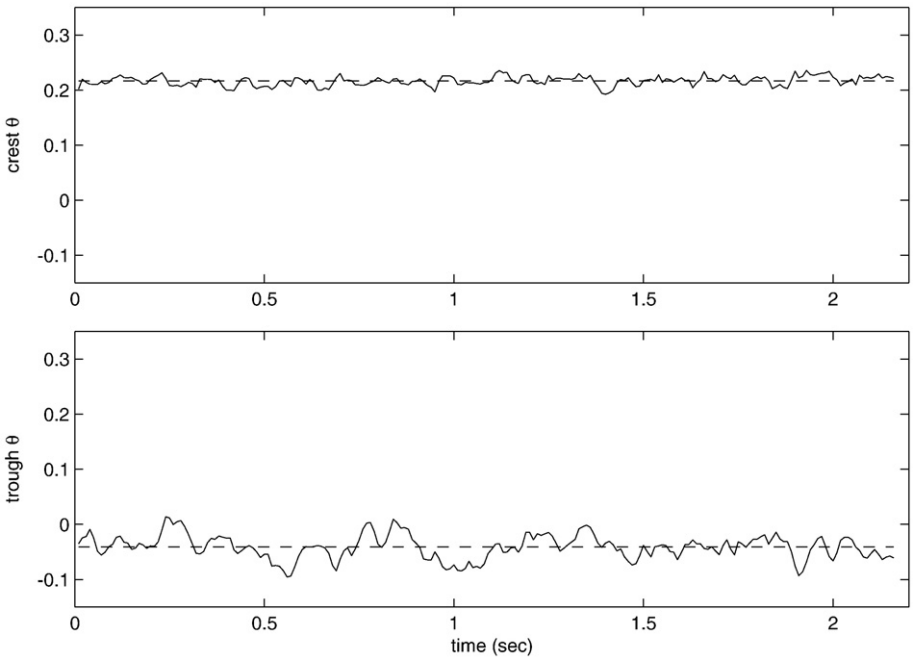

Fig. 12. Shields parameter (nondimensionalized bottom stress) at 2-D ripple crest (upper panel) and ripple trough (lower panel). Two-dimensional ripple with sand grain diameter 0.1 mm (assumed grain size for typical ripple dimension studied here).

Author's personal copy

is apparent that the bottom stress fluctuation is much larger for 3-D ripple case. For the simple power-law type approach adopted here, the instantaneous transport rate is assumed to be completely in-phase with the bottom stress. Because the bottom stress fluctuations are chaotic and despite the instantaneous fluctuating transport rate may be large, the net transport rate due to the fluctuating component of bottom stress is very small. Hence, the net transport rate and migration speed are represented well by the time-averaged component of bottom stress. In reality, it is possible that noticeable amount of sediment transport may not be in-phase with the bottom stress (i.e., suspended load). These suspended sediment transport is further affected by the turbulence structure over the ripples. Therefore, one can expect larger differences for net sediment transport rate and migration speed between the 2-D and 3-D ripples when a more complete sediment transport formulation is implemented.

4. Summary

A well resolved (spatially and temporally) and highly accurate direct numerical simulation (DNS) tool has been developed to understand the fundamental differences in the hydrodynamics of flow over two-dimensional and three-dimensional ripples in a channel geometry and its implications on sediment transport. As a first step, in this paper we focus on the steady flow over the ripples.

The Navier–Stokes equations are solved in the vertical velocity and vertical vorticity formulation. This formulation has the distinct advantage of eliminating the pressure term from the Navier–Stokes equations while requiring the solution of only two governing equations, namely an evolution equation for the Laplacian of the wall-normal velocity and an evolution equation for the wall-normal vorticity. This formulation has reduced storage requirements compared to solutions using the Navier–Stokes equations in primitive variables or in a vorticity transport formulation. In the horizontal x–y directions, periodicity has been assumed and the spatial discretization has been performed using Fourier series expansion, as the flow is statistically homogeneous. In the wall-normal z direction the flow is inhomogeneous, and the flow near the bedforms needs to be well resolved. Without increasing the formal order of accuracy, a high spatial resolution is obtained by resolving the low and high wave-numbers using a fourth order compact finite differences scheme. Immersed boundary techniques have been used to introduce two-dimensional and three-dimensional ripples into the physical domain as a body force term. The simplicity and efficiency of computing in a Cartesian coordinate system is retained. To avoid stringent time step restrictions, a semi-implicit time integration has been implemented to integrate the resultant discretized equations. For the nonlinear terms, an explicit low-storage, three-stage, fourth order Runge–Kutta scheme has been used and for the linear viscous terms, an implicit Crank–Nicholson scheme is used. On applying the time integration scheme to the resultant spatially discretized equations has resulted in Helmholtz- and Poisson-type of equations. These equations are been solved using tridiagonal solvers resulting in the solution of wall-normal velocity and wall-normal-vorticity. Using the continuity condition and the definition of vorticity, streamwise and spanwise velocity components are obtained.

DNS have been performed for two different Reynolds numbers of $Re_\tau = 180$ and 400. The height of the ripples have been kept at a constant value of $H_r/H = 0.2$ (H being the half height of the channel). A detailed analysis of the turbulence statistics and the flow structures has been performed to understand the nature of the differences between the 2-D and 3-D ripples. The presence of ripples shifts the mean velocity away from the wall resulting in the loss of symmetry. Mean velocity scaled by corresponding u_τ revealed that there is no discerning difference between 2-D and 3-D ripples at both $Re_\tau = 180$ and 400. Based on the first order statistics, there are no discernible differences between the 2-D and 3-D ripples.

However, considerable differences are observed for higher-order statistics. Our analysis clearly indicates that large-scale and small-scale features of the flow in the presence of 2-D and 3-D ripples are distinct. Both 2-D and 3-D ripples significantly enhance the peak r.m.s. of velocity and vorticity fluctuations compared to a flat bed. The results indicate that there is a distinct difference in the r.m.s. of velocity fluctuations between the 2-D and 3-D ripples both in vicinity of the bed as well as away from the bed. Further, the effect of 2-D and 3-D ripples is different on r.m.s. of u fluctuations compared to that on the v and w. However, despite significant differences between the 2-D and 3-D ripples are observed in the r.m.s. of vorticity statistics in the vicinity of the ripples, negligible differences are observed in the region away from the bed.

The hydrodynamic analysis has clearly demonstrated that the kinematics of the ripples in addition to the dynamics play an important role in altering the flow dynamics due to the rippled-surface. Hence, the modifications in turbulence statistics (in particular, the higher order statistics) and therefore the resultant flow structures are significantly dependent whether the ripples are two-dimensional or three-dimensional.

The DNS results are further analyzed to study their implication on sediment transport by separating the bottom stress into mean and fluctuating components. The fluctuating component of bottom stress is noticeably larger for 3-D ripple compared to 2-D ripple. The distribution of the bottom stress plays an important role in bed load as well as suspended load. To investigate the significance of having accurate bottom stress distributions from DNS calculations for sediment transport analysis, a simplified sediment transport analysis has been performed to obtain ripple migration speed. Due to simple bedload assumption adopted, the resulting migration speeds for 2-D and 3-D ripples are similar and the effect of fluctuating component of bottom stress on net bedload transport rate appears to be small. However, we believe that accurate bottom stress distribution obtained from the DNS will play a critical role in future studies towards more accurate analysis of suspended sediment transport.

In conclusion, the importance of this work is three folds: (1) a robust DNS tool to simulate flow over 2-D and 3-D ripples has been developed. The Navier Stokes equations are solved in vertical-velocity and vertical-vorticity formulation, (2) analysis has been performed to better understand the differences in the hydrodynamics and its implications to sediment transport for 2-D and 3-D ripples, and finally, (3) the importance of fluctuating component of bottom-stress in relation to the mean components and its implication to the sediment transport is explored using a simple sediment transport analysis. Considerable differences between 2-D and 3-D ripples are observed for higher order turbulent flow statistics. The prediction of higher order statistics is important for several critical coastal applications, such as suspended load transport. We believe these findings summarized above are important to coastal applications and provide good guideline to further extend this DNS tool for suspended load or gas/nutrient transport across the seabed with bedforms. This study demonstrates results of $Re_\tau = 400$ (higher than prior studies of Re_τ of 180) and feasibility of using DNS to study coastal problems in the future. The robust DNS tool that has been developed as a part of this work coupled with more complicated sediment transport models in the near future is an important direction for more process-based prediction of coastal sediment transport.

In the ocean, as the forcing is due to current and waves, in our future work we will focus on oscillatory flow over 2-D and 3-D ripples, and study the differences in sediment transport rate and the ripple migration speed. Further, as the sediment transport may not be in-phase with the bottom stress, suspended load transport is further affected by the turbulence structure over the ripples. Therefore, one can expect larger differences for net sediment transport rate and migration speed between the 2-D and 3-D ripples when a more complete sediment transport formulation is used.

Author's personal copy

Acknowledgements

Bhaganagar would like to acknowledge financial support provided by Maine Space Grant Consortium and Hsu would like to acknowledge National Science Foundation (OCE-0644497; CBET-0426811).

References

Amsler, M.L., Garcia, M.H., 1997. Sand dune geometry of large rivers during flood. J. Hydraul. Eng. 123, 582–584.
Andersen, K.H. 2000, The Dynamics of Ripples Beneath Surface Waves and Topics in Shell Models of Turbulence. Ph.D. thesis Niels Bohr Institute, University of Copenhagen.
Antonia, R.A., Krogstad, P.A., 2001. Return to isotropy for rough case using Lumley's triangle. Fluid Dyn. Res. 28, 139–157.
Ardhuin, F., Drake, T.G., Herbers, H.C., 2002. Observations of wave-generated vortex ripples on the North Carolina continental shelf. J. Geophys. Res. 107 (C10) (Art. No. 3143).
Ashrafian, A., Andersson, H.I., Manhart, M., 2004. DNS of turbulent flow in a rod-roughened channel. Int. J. Heat Fluid Flow 25 (3), 373–383.
Ashworth, P.J., Best, J.L., Roden, J.E., Bristow, C.S., Klaassen, G.J., 2000. Morphological evolution and dynamics of a large, sand braid-bar, Jamuna River, Bangladesh. Sedimentology 47, 533–555.
Baas, J.H., Koning, H., 1995. Washed-out ripples: their equilibrium dimensions, migration rate, and relation to suspended-sediment concentration in very fine sand. J. Sediment. Res. A65 (2), 431–435.
Bandyopadhyay, R., Watson, R.D., 1988. Structure of rough-wall turbulent boundary layers. Phys. Fluids 31, 1877–1880.
Barr, B.C., Slinn, D.N., Pierro, T., Winters, K., 2004. Numerical simulation of turbulent oscillatory flow over sand ripples. J. Geophys. Res. 109 (C9).
Best, J.L., 2005. The fluid dynamics of river dunes: a review and some future research directions. J. Geophys. Res. 110.
Benney, D.J., Gustavsson, L.H., 1981. A new mechanism for linear and nonlinear hydrodynamic instability. Stud. Appl. Math 64, 185–209.
Bhaganagar, K., Rempfer, D., Lumley, J.L., 2002. Direct numerical simulation of spatial transition to turbulence using fourth-order vertical velocity second-order vertical vorticity formulation. J. Comp. Physiol. 180, 200–228.
Bhaganagar, K., Kim, J., Coleman, G., 2004. Effects of roughness on wall-bounded turbulence. Flow Turbul. Combust. 72, 463–492.
Bhaganagar, K., Coleman, G., Kim, J., 2007. Effect of roughness on pressure statistics. Phys. Fluids 19 (2).
Calantoni, J., Holland, K.T., Drake, T.G., 2005. Modelling sheet-flow sediment transport in wave-bottom boundary layers using discrete-element modelling. Philos. Trans. R. Soc. Lond. A 362, 1987–2001.
Calhoun, R.J., Street, R.L., 2001. Turbulent flow over a wavy surface: neutral case. J. Geophys. Res. 106 (C5).
Canuto, C., Hussaini, M.Y., Quarteroni, A., Zang, T.A., 2000. Spectral methods in fluid dynamics. Springer series in computational science and Engineering, Springer-Verlag, New York.
Carpenter, M.H., Kennedy, C.A., 1994. A fourth order 2N-storage Runge–Kutta scheme. NASA Tech. Memo. 109112.
Chang, Y.S., Hanes, D.M., 2004. Suspended sediment and hydrodynamics above mildly sloped long wave ripples. J. Geophys. Res. 109, C07002.
Chang, Y.S., Scotti, A., 2003a. Modeling unsteady turbulent flows over ripples: Reynolds-averaged Navier–Stokes equations (RANS) versus large-eddy simulation (LES). J. Geophys. Res. 109, C09012.
Chang, Y.S., Scotti, A., 2003b. Entrainment and suspension of sediments into a turbulent flow over ripples. J. Turbul. 4, 1–22.
Cheng, H., Castro, I.P., 2002. Near wall flow over urban-like roughness. Boundary-Layer Meteorol. 229–257.
Cherukat, P., Na, Y., Hanratty, T.J., 1998. Direct numerical simulation of a fully developed turbulent flow over a wavy wall. Theor. Comput. Fluid Dyn. 11, 109–134.
De Angelis, V., Lombardi, P., Banerjee, S., 1997. Direct numerical simulation o turbulent flow over a wavy wall. Phys. Fluids 9 (8), 2429–2442.
Engelund, F., Fredsøe, J., 1976. A sediment transport model for straight alluvial channels. Nord. Hydrol. 7, 293–306.
Fadlun, E.A., Verzicco, R., Orlandi, P., Mohd-Yusof, J., 2000. Combined immersed-boundary/finite-difference methods for three-dimensional complex flow simulations. J. Comput. Phys. 161, 35–60.
Fredsøe, J., Andersen, K.H., Sumer, B.M., 1999. Wave plus current over a rippled-covered bed. Coast. Eng. 38, 177–221.
Fredsøe, J., Sumer, B.M., Kozakiewicz, A., Chua, L.H.C., Deigaard, R., 2003. Effect of externally generated turbulence on wave boundary layer. Coast. Eng. 49, 155–183.
George, J., Simpson, R.L., 2000. Some effects of sparsely distributed three-dimensional roughness elements on two-dimensional turbulent boundary layers. AIAA Pap. 2000-0915.
Goldstein, D., Handler, R., Sirovich, L., 1993. Modeling a no-slip flow boundary with an external force field. J. Comp. Phys. 105, 354–366.
Grant, W.D., Madsen, O.S., 1979. Combined wave and current interaction with a rough bottom. J. Geophys. Res. 84 (C4), 1797–1808.
Grant, W.D., Madsen, O.S., 1981. Movable bed roughness in unsteady oscillatory flow. J. Geophys. Res. 87 (NC1), 469–481.
Hanes, D.M., Alymov, V., Chang, Y.S., Jette, C., 2001. Wave-formed sand ripples at Duck, North Carolina. J. Geophys. Res. 106 (C10), 22,575–22,592.
Henn, D., Sykes, R.I., 1999. Large-eddy simulation of flow over wavy surfaces. J. Fluid Mech. 383, 75–112.
Hsu, T.-J., Jenkins, J.T., Liu, P.L.F., 2004. On two-phase sediment transport: sheet flow of massive particles. Proc. R. Soc. Lond. (A) 460 (2048), 2223–2250.
Hudson, J.D., Dykhno, L., Hanratty, T.J., 1996. Turbulence production in flow over a wavy wall. Exp. Fluids 20, 257–265.
Jensen, B.L., Sumer, B.M., Fredsøe, J., 1989. Turbulent oscillatory boundary-layers at high Reynolds numbers. J. Fluid Mech. 206, 265–297.
Kuhlborn, J.M., 1993, Wachstum und wanderung von sedimentriffeln, PHD dissertation, Fachbereich Bauingenierurwesen, Techn. Hochschule Darmstadt, Germany (in German).
Lele, S.K., 1992. Compact finite difference schemes with spectral like resolution. J. Comput. Phys. 103, 16–42.
Mantz, P.A., 1978. Bedforms produced by fine, cohesionless, granular and flakeysediments under subcritical water flows. Sedimentology 25, 83–103.
Mathisen, P.P., Madsen, O.S., 1996. Wave and currents over a fixed rippled bed I. bottom roughness experienced by waves in the presence and absence of currents. J. Geophy. Res. 101 (C7), 16533–16542.
McLean, S.R., Smith, J.D., 1979. Turbulence measurements in the boundary layer over a sand wave field. J. Geophys. Res. 84, 7791–7808.
McLean, S.R., Nelson, J.M., Wolfe, S.R., 1994. Turbulence structure over two-dimensional bed forms: implication for sediment transport. J. Geophys. Res. 99 (6), 12729–12747.
Meyer-Peter, E., Muller, R., 1948. Formulas for bed load transport, paper presented at Second Congress, Int. Assoc. for Hydraul. Res., Rotterdam, Netherlands.
Parsons, D.R., Best, J.L., Orfeo, O., Hardy, R.J., Kostaschuk, R., Lane, S.N., 2005. Morphology and flow fields of three-dimensional dunes, Rio Parana, Argentina: results from simultaneous multibeam echo sounding and acoustic Doppler current profiling. J. Geophys. Res. 110, F04S03.
Perry, A.E., Lim, K.L., Henbest, S.M., 1987. An experimental study of the turbulence structure in smooth- and rough-wall boundary layers. J. Fluid Mech. 177, 437–466.
Pope, S.B., 2000. Turbulent Flows. Cambridge University Press.
Raudkivi, A.J., 1997. Ripples on stream bed. J. Hydraul. Eng. 123 (1), 58–64.
Raupach, M.R., Antonia, R.A., Rajagopalan, S., 1991. Rough-wall turbulent boundary layers. Appl. Mech. Rev. 44 (1), 1–20.
Rist, U., Fasel, H., 1995. Direct numerical simulation of controlled transition in a flat-plate boundary layer. J. Fluid Mech. 298, 211–248.
Scandura, P., Vittori, G., Blondeaux, P., 2000. Three-dimensional oscillatory flow over steep ripples. J. Fluid Mech. 412, 355–378.
Sen, M., Bhaganagar, K., Juttijudata, V., 2007. Application of proper orthogonal decomposition to investigate a turbulent boundary layer in a channel with rough walls. J. Turbul. 8 (41), 1–22.
Tjerry, S., Fredsøe, J., 2004. Calculation of dune morphology. J. Geophys. Res. 110, F04013.
Traykovski, P., Hay, A.E., Irish, J.D., Lynch, J.F., 1999. Geometry, migration and evolution of wave orbital ripples at LEO-15. J. Geophys. Res. 104 (C1), 1505–1524.
Van, R.L.C., 1984. Sediment transport, Part II: Suspended load transport. J. Hydraul. Eng, vol. 110(11). ASCE, pp. 613–1641.
Wiberg, P.L., Harris, C.K., 1994. Ripple geometry in ripple-dominated environments. J. Geophys. Res. 99 (C1), 775–789.
Williamson, J.H., 1980. Low-storage Runge–Kutta schemes. J. Comp. Phys. 35 (48), 48–56.
Yue, W., Lin, C.-L., Patel, V.C., 2005. Coherent structures in open-channel flows over a fixed dune. J. Fluids Eng. 127, 858–864.
Yusof, M.J., 1997. Combined immersed-boundary/B-spline methods for simulations of flow in complex geometries. CTR-Annual Research Briefs - Stanford Univ./NASA Ames.
Zedler, E.A., Street, R.L., 2001. Large-eddy simulation of sediment transport: currents over ripples. J. Hydraul. Eng. 127 (6), 444–452.
Zedler, E.A., Street, R.L., 2006. Sediment transport over ripples in oscillatory flow. J. Hydraul. Eng. 132 (2), 180–193.